

Experimental Study of the Interaction between a Turbulent Flame and a Cooling Air Film

Sylvain Petit¹, Antoine Blaise¹, Gilles Godard¹, Bruno Mille¹, Thierry Muller¹, Philippe Toutain¹, Frédéric Grisch¹, Pradip Xavier^{1,*}

¹: Normandie Univ, UNIROUEN, INSA Rouen, CNRS, CORIA, 76000 Rouen, France

*Corresponding author: pradip.xavier@coria.fr

Keywords: Flame-cooling air interaction, Flame dynamics, PIV, OH-PLIF, Phosphor thermometry

ABSTRACT

Electric hybridization appears to be a promising technological pathway to mitigate CO₂ emissions in the aviation sector. Yet, this solution requires to develop high-density compact aeronautical gas turbine combustors. Thus, wall thermal management is becoming more critical. It is known that combustor walls are commonly cooled with the use of a parietal air film so that flame-cooling air interaction (FCAI) processes are likely to increase the level of complexity compared to a classical flame-wall interaction configuration. The current experimental study is focused on the analysis of the interactions between a V-shaped lean turbulent premixed methane-air flame and a parietal cooling air film generated by means of a splash-cooling system. The blowing ratio is used as the primary parameter that is varied in order to investigate the flame dynamics. Experiments are carried out in a new lab-scale test rig operating at atmospheric pressure. The mainstream produces turbulent flames classified into wrinkled flamelets. The flame structure, the reactive aerodynamics and the wall temperature are simultaneously studied by implementing planar laser-induced fluorescence of the OH radical (OH-PLIF), reactive particle image velocimetry (PIV) and surface intensity-ratio phosphor thermometry (PT). Results show that the mean flow field and the mean flame topology significantly differs according to the level of blowing ratio. Further joint correlations of experimental measurements highlight various FCAI regimes. For blowing ratios below unity, a common flame-wall interaction process occurs and the air film has a limited influence on the flame dynamics. Increasing the blowing ratio enables to establish a cooling air film at the wall. Though it effectively increases the level of thermal protection, it does not have much influence on the flame topology. Eventually, for larger blowing ratios, the flame dynamics is piloted by the shear layer dynamics, associated with strong flow strain. The flame is pushed away from the wall and is located in the outer region of the shear layer. The cooling effectiveness is not improved anymore and shows no more dependencies with the blowing ratio.

1. Introduction

Despite the numerous incentives to fasten the energetic transition (e.g. the flightpath 2050 goals from ACARE: 75% reduction in carbon dioxide emissions by 2050), the current impact of the latest

propulsion and power technologies in the aviation sector will certainly fall short by 2035. Thus, aero-engine manufacturers must establish a technological roadmap to prioritize the emergence of radical low-carbon technologies. Among others, downsized high-power density core engines made of lighter materials can be a solution in order to obtain electrical-hybrid engines. Even though these new architectures would be beneficial for the overall propulsion efficiency, it would also induce additional concerns on the material durability. Hence, it is of primary importance to address the technological challenges regarding wall thermal management by studying the interrelated physical processes (i.e. thermal, chemical or aerodynamics) between a flame, a wall and a cooling technology.

Near-wall combustion has been extensively studied in the combustion community (Poinsot et al., 2011; Dreizler & Böhm, 2015). Because combustor walls are colder (~ 1000 K) than flame/burnt gases temperatures (~ 2500 K), heat transfer in the order of MW/m^2 occurs between the flow and the wall. This creates enthalpy losses in a thin near-wall region, which modifies the thermochemical state of the fluid (Mann et al., 2014; Jainski et al., 2017). The wall-bounded aerodynamics also influences the flame dynamics through strain and curvature (Bruneaux et al., 1996; Foucher et al., 2003) while the flame can retro-act on the flow field (Alshaalan & Rutland, 2002; Gruber et al., 2010). When the flame is ultimately quenched, heat is transferred to the wall (Sotton et al., 2005). In this near-wall region, transport processes are more preponderant than heat production (Ganter et al., 2017; Zentgraf et al., 2021). Near-wall combustion investigations are usually divided into two generic configurations: head-on quenching (HOQ) where the flame impinges normal to the wall and side-wall quenching (SWQ) when the flame propagates parallel to the wall. Nevertheless, near-wall combustion in real engines is more complex: walls in aero-engine combustors are commonly cooled, acting as a thermal protective method to improve the wall thermal resilience (Lefebvre & Ballal, 2010). Effusion cooling is the most widespread method, which consists in thousands of small holes (≈ 0.5 mm) drilled into the wall, enabling the injection of small air jets which coalesce to form a thin shielding air-film (Kumar et al., 2020). This protective cooling method is expected to drastically change the flow topology, with the presence of a shear layer and the generation of new coherent turbulent structures (Mendez & Nicoud, 2008). Moreover, the heterogeneous mixing between the reactive flow and the cooling air can modify the flame structure, produce secondary reaction zones (Fischer et al., 2021), or impact the wall cooling effectiveness (Ahmed et al., 2021). In order to underpin the above interconnected phenomena occurring near walls in aero-engine combustors, various simplified cases have been developed (Behrendt et al., 2008), including isothermal and non-reacting low-pressure test rigs (Gustafsson & Johansson, 2001), or non-isothermal benches (Picchi et al., 2020). Investigations of direct flame-film cooling interactions are scarce due to the improved level of complexity (Feist et al., 2003; Lange et al., 2012), but have received more attention recently.

A joint experimental and numerical research at a fundamental level has been reported to reproduce the physics of flame-cooling air interaction (FCAI), with a focus on the near-wall CO emissions (Rivera et al., 2019; Palulli, Talei, & Gordon, 2021; Palulli, Brouzet, et al., 2021). Rivera et al.

(2019) conducted global measurements consisting in flame visualization and CO measurements in the exhaust with the presence of single wall coolant jet. They highlighted a reduction in CO emissions due to a better oxygenation. The same configuration was numerically investigated and showed the importance of the blowing ratio parameter on the flame dynamics (Palulli, Talei, & Gordon, 2021). Turbulence was accounted for with a series of coolant jets, and mixing between the reacting flow and the cooling air results in a longer flame and reduced CO mass fractions. To increase the level of complexity, a high-pressure, high-temperature optically-accessible single-sector gas turbine swirled combustor was developed with the insertion of an effusion plate (Hermann et al., 2019). The qualitative analysis of OH fields and conditional averaging of velocity fields reveal an important near-wall activity with various interaction mechanisms between the cooling air film and the burnt gases (Greifenstein et al., 2019).

There is a clear lack of knowledge on the various FCAI processes. Though the valuable highlights reported in the recent studies, the behavior of the flame front remains unclear with the presence of a cooling air film. For instance, Greifenstein & Dreizler (2021) investigated the role of mixing but could not provide insights on how the cooling air film could directly affect the flame dynamics. This study presents an experimental investigation of a lean methane-air turbulent flame interacting with a parietal cooling air film. Planar-induced fluorescence of OH (OH-PLIF), reactive particle image velocimetry (PIV) and surface phosphor thermometry (PT) are simultaneously performed to analyze the wall-flow-flame interactions.

2. Experimental methods

2.1. Test rig

In order to observe the near-wall flame topology, an experimental combustion test bench CENTOR (combustion test bench to observe near-wall energy processes) operating under atmospheric pressure has been developed at CORIA. Dry air and methane are controlled with thermal mass flow controllers (Bronkhost) and injected at the bottom of a plenum in order to produce a premixed mixture with an homogeneous velocity profile. After passing sequentially through a porous, plate, a perforated grid (hole diameter of 2 mm), a 58 mm layer of glass balls (5 mm in diameter), and a 50 mm height metallic honeycomb, the methane-air mixture is guided into a convergent nozzle equipped with a multi-grid turbulence generator (series of three perforated plates) which generates a 10-15% turbulence intensity in the streamwise direction (Mazellier et al., 2010). The flow is guided to a water-cooled optically accessible 80 mm × 80 mm squared-section confined module. A V-shaped flame is stabilized on a 4 mm ceramic rod located downstream of the turbulence grid. One branch of the flame impinges on a thermally-controlled stainless steel wall equipped with a splash-cooling slot device (Lefebvre & Ballal, 2010; Bogard & Thole, 2006). Contrary to current effusion-based film cooling liners, this one enables to produce an air film less dependent on geometrical considerations (e.g. hole patterns, porosity, hole angle). Dry air is fed into a 12 mm × 50 mm plenum. The cooling air is bled into a 2 mm × 70 mm × 10 mm open-ended mixing volume through

a row of 21 holes (diameter of 1 mm, length of 2 mm, 2 mm spacing) and deflected along the inner wall surface of the combustor by means of a 0.5 mm thick lip (Sivasegaram & Whitelaw, 1969). The mixing volume and the lip enable to coalesce the air jets into a continuous film, but they introduce a 2.5 mm protrusion into the mainstream. Exhaust gases are flushed out by two lateral chimneys. An horizontal air-cooled zenithal quartz window is inserted in the chimney section, allowing to obtain a passage for the laser sheets, being perpendicular to the wall.

2.2. Operating conditions

A single operating condition in the mainstream is considered in the current study. The main mass flow rate is set to $\dot{m}_m = 22$ g/s with an equivalence ratio, $\phi = 0.9$, resulting in an averaged Reynolds number, $Re = 15500$, estimated by using the nozzle exit section. The thermal power is maintained to 57.5 kW. The laminar burning velocity, the thermal flame thickness and the adiabatic flame temperature of this operating condition are $S_L^0 = 0.33$ m/s, $\delta_{th} = 1$ mm and $T_{ad} = 2230$ K (calculated with Cantera (Goodwin et al., 2021))

The blowing ratio M is used as the main aerodynamic flow parameter to characterize the interaction between the cooling air-film and the main inflow conditions,

$$M = \frac{(\rho \bar{u}_y)_j}{(\rho \bar{u}_y)_m}, \quad (1)$$

where $(\cdot)_j$ stands for the air film and $(\cdot)_m$ is for the mainstream. M is varied from 0.5 up to 3. The temperature of the two streams is set to 298 K while the wall temperature is set to 423 K.

2.3. Laser diagnostics

In order to assess the flame dynamics, the reactive flow aerodynamics, and the wall temperature, three optical-based diagnostics are simultaneously implemented (Fig. 1).

2.3.1. Flame dynamics

The interface between fresh and burnt gases is detected by using planar laser-induced fluorescence on the hydroxyl radical (OH), produced in the flame reaction zone and present in the burnt gases. OH radicals are excited via the $Q_1(5)$ ro-vibrational transition (282.75 nm) of the $A^2\Sigma^+(\nu' = 1) \leftarrow X^2\Pi(\nu'' = 0)$ OH band, using a tunable dye laser (Quantel TDL90) pumped by a Nd:YAG laser operating at 10 Hz. The laser beam is shaped into a 30 mm in height laser sheet (spherical $f = +1500$ mm, cylindrical $f = -50$ and $+400$ mm, Fig. 1), and is aligned perpendicular to the wall by means of the zenithal optical window. The laser sheet presents a slight angle relative to the wall, for probing the near-wall OH radical, resulting in a 20 mm \times 100 mm region of interest (ROI). Fluorescence signals are collected with an ICCD camera (PI-MAX 3). It is equipped with a $f/2.8$

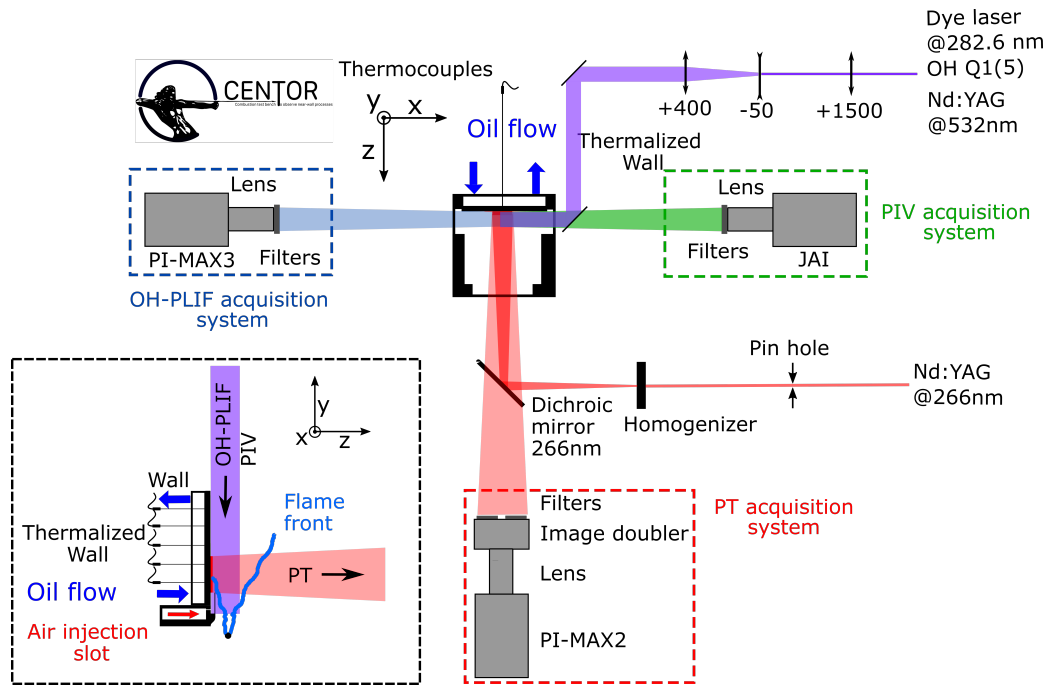


Figure 1. Top view of the experimental arrangement. The CENTOR burner is visible at the center along with the different optical diagnostics: particle image velocimetry (PIV) and OH planar laser-induced fluorescence (OH-PLIF) share the same optical excitation path (violet) while the collection systems are located on both sideways of CENTOR (blue and green). Surface phosphor thermometry is implemented in a backward scattering configuration (red). The inset shows a lateral view of the wall, where the splash-cooling air system is visible.

105 mm UV-Cerco lens and a narrow optical band-pass filter (Asahi Spectra, 310 ± 10 nm). No interferences with the flame nor phosphorescence is noticeable during experiments. The camera exposure time is set to 80 ns, while the acquisition starts 5 ns prior to the laser pulse. 1000 single-shot fluorescence images are acquired for each operating point, which are subsequently background subtracted and normalized. A progress variable, c , is estimated by binarizing the OH images to separate fresh ($c = 0$) from burnt gases ($c = 1$). Similarly to Zentgraf et al. (2021), a supplementary threshold on the normalized OH gradient normal to the OH boundary is applied to segment the interface into two parts: the flame front (FF) and a fresh-burnt gases interface (F-BGI).

2.3.2. Flow dynamics

Particle image velocimetry (PIV) is implemented to characterize the flow field. Zirconium dioxide solid particles (ZrO_2 , nominal diameter of $5 \mu\text{m}$) are seeded into the mainstream and the cooling air film by means of two fluidized bed seeding systems. The Stokes number is estimated to be between 0.005 and 0.2 depending on the operating condition, which ensures that particles are correctly carried by the fluid. A dual-cavity frequency-doubled Nd:YAG laser (Quantel Twin Ultra) operating at 532 nm is used for the double-pulse generation, with a time separation of $30 \mu\text{s}$. The laser beam is shaped with the same optics used for the OH-PLIF. The superimposition of the focusing point of both laser sheets is ensured by placing a beam expander on the PIV beam laser.

The ROI of the technique is $25\text{ mm} \times 130\text{ mm}$. Images are collected on a Jai RM 4200-CL CCD sensor equipped with a $f/2.8$ 50 mm Ziess lens. A narrow band-pass optical filter ($532 \pm 10\text{ nm}$) is inserted to only collect the Mie scattering of the seeded particles. 1000 images are collected for each operating condition, subsequently background-subtracted. Velocity fields are estimated with a multipass adaptive-windowing cross correlation algorithm (Dantec 6.9), resulting in a final $32\text{ pix} \times 32\text{ pix}$ interrogation window and a 50% overlap. The vector spacing is 1 mm and the uncertainty is estimated to be approx. 0.5 m/s (sub-pixel interpolation error of 0.25 pix).

2.3.3. Wall temperature

Two-dimensional surface phosphor thermometry is implemented with the manganese-activated magnesium fluorogermanate phosphor powder, $\text{Mg}_4\text{FGeO}_6:\text{Mn}$ (MFG, Osram SV067) (Aldén et al., 2011). A 5% in mass of MFG particles are mixed with a water-based binder (Zyp Coatings HPC), and coated on the wall surface by using an air-brush. The phosphor coating thickness is measured with an electromagnetic thickness gauge (Sauter TE 1250-0.1FN) and remains lower than $10\text{ }\mu\text{m}$. The fourth harmonic of a Nd:YAG laser at 266 nm (Quantel Qsmart 450) is used with a repetition rate of 10 Hz to excite the phosphor particles. The laser beam is shaped into a top-hat diffuser (Holo/Or) and a dichroic mirror reflects the laser beam towards the coated wall to obtain a $28\text{ mm} \times 28\text{ mm}$ ROI. The phosphorescence images are collected with an ICCD camera (PI-MAX2) connected to a lens (Cercor, $f/2.8$ 105 mm) and an image doubler (Lavisision). Spectral phosphorescence bands are selected with two colored bandpass filters ($680\text{ nm} \pm 20\text{ nm}$ and $658\text{ nm} \pm 20\text{ nm}$). Rationing of images is correlated to temperature with a calibration step performed with an open tubular furnace (Nabertherm RHTH 80-300) between 300 and 850 K. 1000 instantaneous images are acquired for each operating condition. A streamwise profile of wall temperature is extracted in accordance with the OH-PLIF and PIV measurements. To avoid any interferences, the phosphorescence excitation and collection start $80\text{ }\mu\text{s}$ after the OH collection.

3. Results

3.1. Influence of the blowing ratio M

Figure 2 presents the normalized mean velocity magnitude fields (blue-to-red color scale), flame location (black iso-contours) and wall temperature (yellow line), for various blowing ratios M . The mean progress variable $\bar{c} = 0.25$ (red dashed line in Fig. 2) is estimated with OH data, by averaging all instantaneous fields that have been binarized to distinguish fresh and burnt gases. Note that no PIV data are available in the vicinity of the lip due to an intense reflection (a physical mask is inserted near the burner). The flow field far away from the wall is barely affected by the presence of the cooling air film. Nevertheless, the increase of the blowing ratio M clearly modifies the near-wall aerodynamics, with a large region of high velocities for $M = 3$, Fig. 2(c). The mean progress variable shows the sole location of the flame front (FF) and the fresh-burnt gases interface

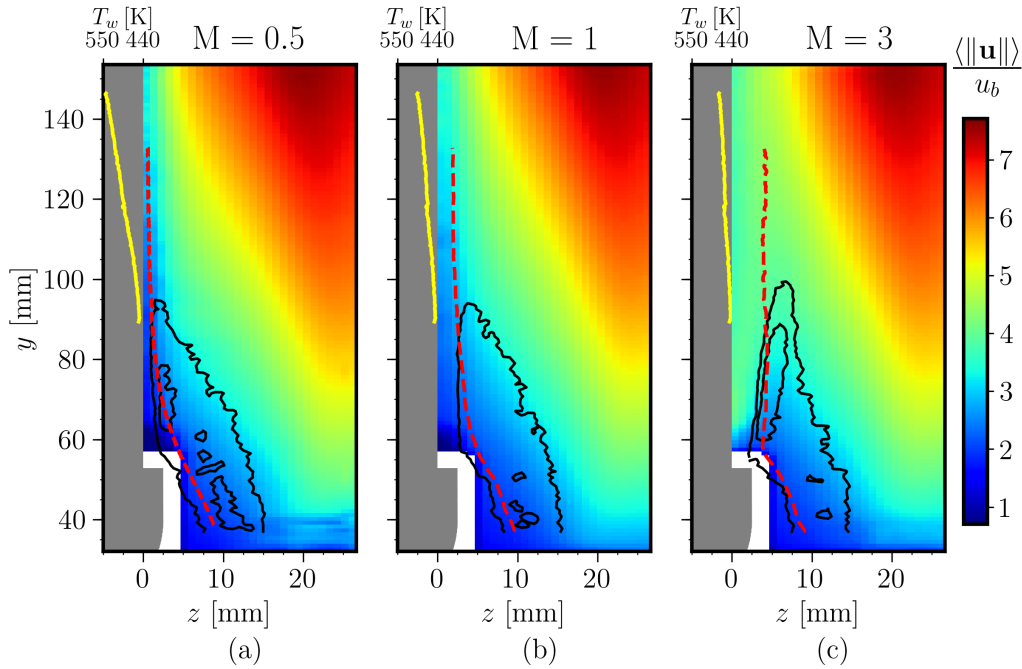


Figure 2. Normalized mean velocity magnitude field (blue-to-red color scale), mean OH interface depicted by the progress variable $\bar{c} = 0.25$ (red dashed line), flame brush probability (black contours) and mean wall temperature (yellow line) for three blowing ratios: (a) $M = 0.5$, (b) $M = 1$ and (c) $M = 3$.

(F-BGI) of the left branch of the flame. The latter comes very close to the wall for $M = 0.5$, with an impingement region varying from 95 to 130 mm. The V-shaped flame branch is bended while being convex towards the wall. The cooling air momentum is not large enough to counteract the propagation of the turbulent flame towards the wall. When $M = 1$, Fig. 2(b), the interface is displaced from the wall, with a minimum wall distance being approximately similar to the lip protrusion (2.5 mm). The flame is less curved, and is almost parallel to the wall for $y > 100$ mm. When $M = 3$, the air film is clearly visible but not fully established at the exit of the lip. The interface is located further away from the wall ($z > 2.5$ mm) and presents an inflection point nearby the lip ($y \approx 55$ mm) to be concave towards the wall. The air film has enough momentum to interact rapidly with the flame and pushes it away from the wall.

Individual flame fronts (FF) are reported via a flame brush probability (black contours in Fig. 2), and have a similar shape for $M = 0.5$ and $M = 1$. The flame brush is wider near the wall, with a near-wall impingement region ranging from $y = 55$ to 100 mm. The good alignment between the flame brush contour and \bar{c} (red dashed line) proves that the FF and the F-BGI form a continuous boundary through the flame tip (i.e. highest point of the flame brush). The flame brush that is possibly interacting with the air film presents a strong deflection towards the burner centerline for $M = 3$ (Fig. 2c). The FF is rather well aligned with \bar{c} above the lip while there is a slight misalignment in the vicinity of the flame tip, highlighting a more complex FF topology.

The averaged wall temperature, T_w (yellow lines), in Fig. 2 shows a quasi-linear vertical positive gradient for all blowing ratios. As expected, this gradient is reduced when M increases, due to the

improved benefits of the cooling air film. When inspecting the height of the flame brush, the direct contact of the burnt gases with the wall may be important in the parietal heat transfer.

3.2. Wall thermal stress

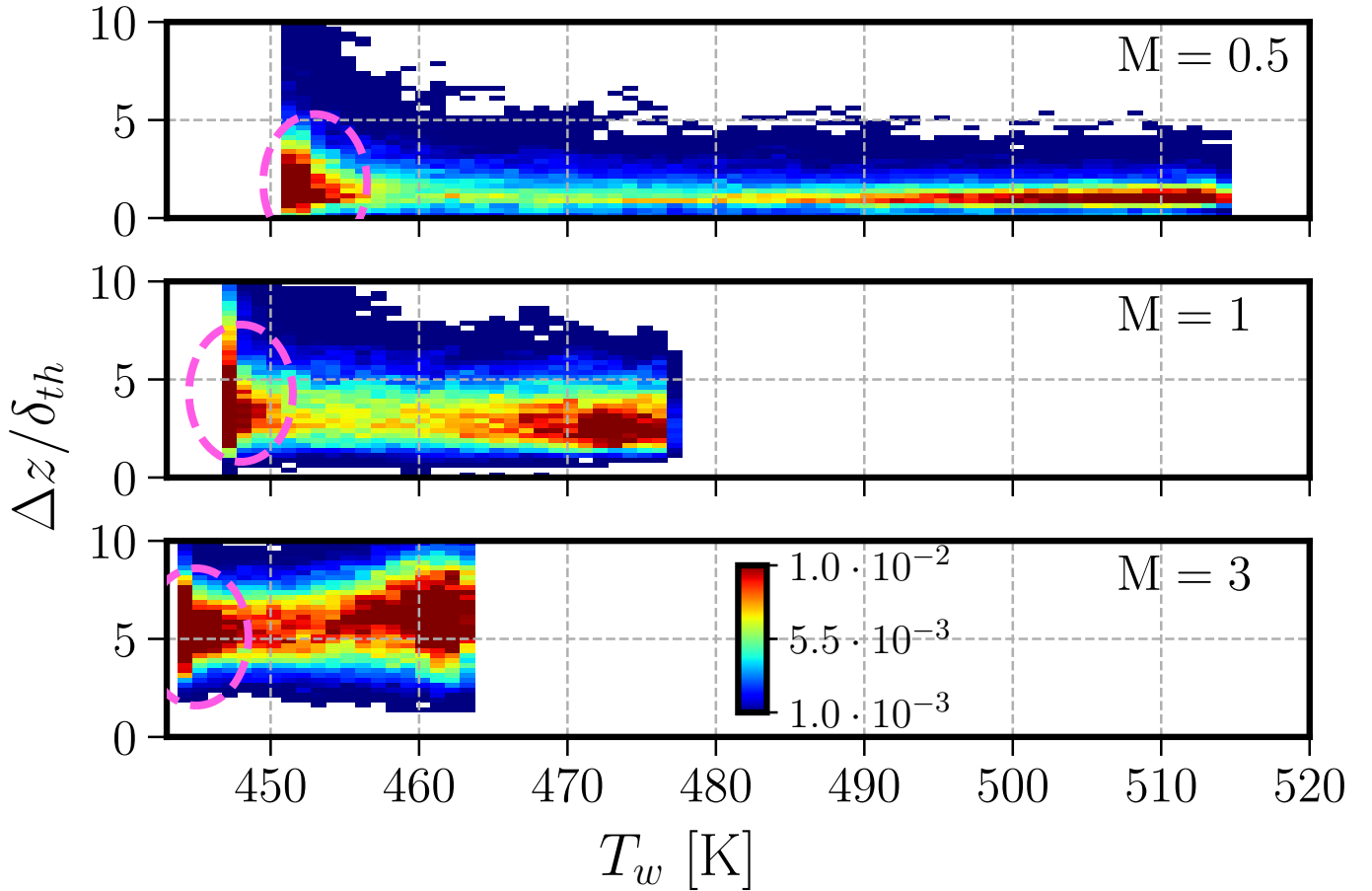


Figure 3. Joint PDFs between the wall temperature, T_w , and the normalized distance to the wall of the FF+F-BGI interface, $\Delta z/\delta_{th}$, for $M = 0.5$, $M = 1$ and $M = 3$.

The wall temperature distribution, T_w , is jointly correlated with the normalized wall distance of the FF+F-BGI interface, $\Delta z/\delta_{th}$, in Fig. 3. The mean value of T_w and its fluctuations are reduced when M increases, proving the better thermal control of the air film. The strong correlation between T_w and $\Delta z/\delta_{th}$ is evidenced with two high-probability regions for all M . The first one is located at low temperature with a round lobe for all M (magenta dashed circles in Fig. 3) and corresponds solely to the FF (not shown). For $M = 0.5$, the values of $\Delta z/\delta_{th}$ feature a predominance of head-on quenching scenarios, in agreement with classical Peclet quenching numbers (Poinsot et al., 2011; Zentgraf et al., 2021). This region moves away from the wall with the air film. The second region at higher T_w is related to the F-BGI and evolves with M . The presence of burnt gases close to the wall combined with the diminishing air film momentum explains the large horizontally-elongated region for $M = 0.5$. Conversely, increasing M shrinks this region due to continuous presence of the

air film, and results in more uniform T_w levels. For $M = 3$, a new rounded lobe is observed, being slightly shifted away from the wall compared to the first lobe.

3.3. Interaction of the cooling air film on the flame dynamics

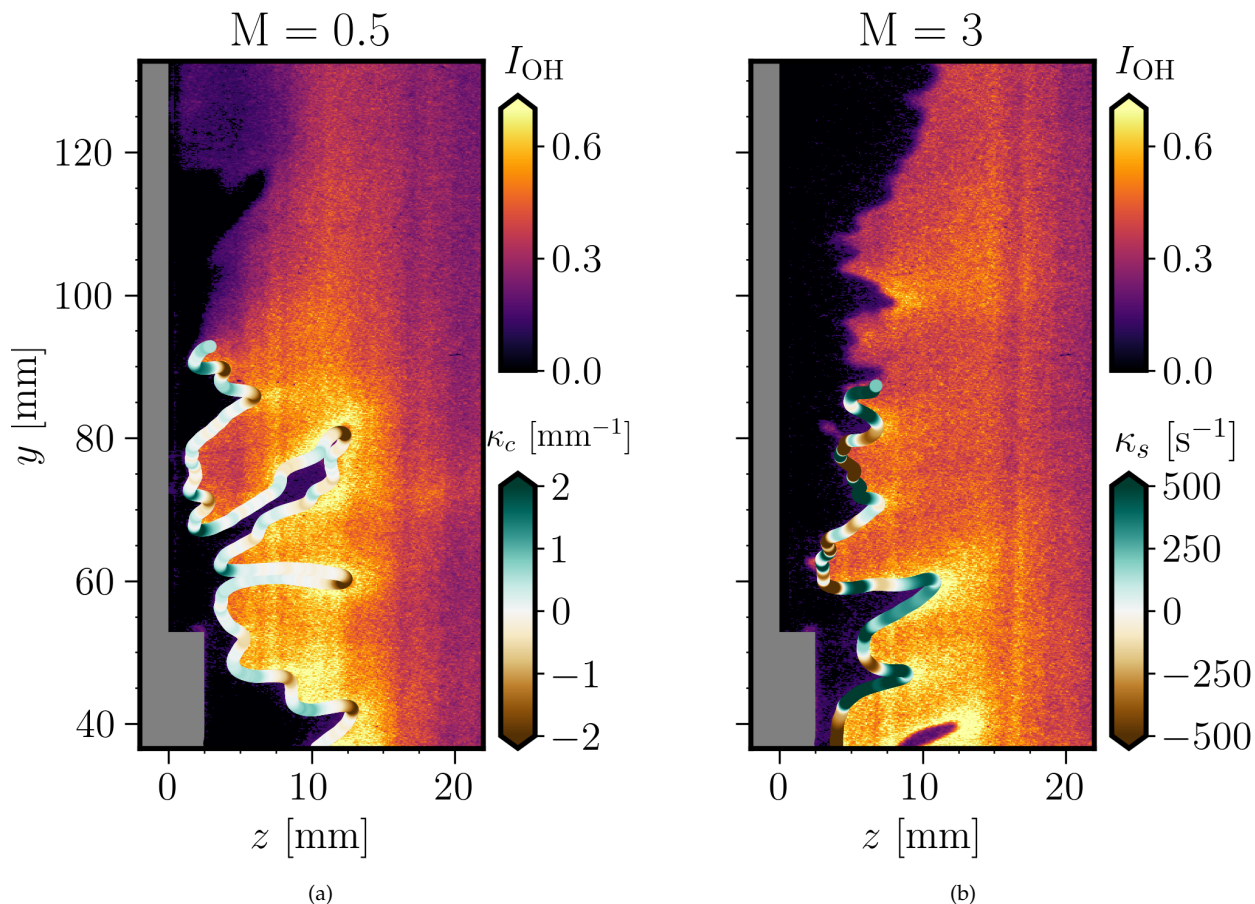


Figure 4. Instantaneous OH-PLIF signals (black-to-yellow color scale) with the identification of the flame front (FF) colored by (a) flame curvature, κ_c (Eq. 2), for $M = 0.5$ and (b) flame strain, κ_s (Eq. 3), for $M = 3$ (brown-to-green color scale).

Instantaneous flame fronts are shown in Fig. 4 for two blowing ratios. Although OH fields present a clear stiff intensity gradient between fresh and burnt gases, the inspection of the normal-to-the-flame OH intensity presents a region with higher levels in the burnt gases for $y < 90$ mm. In contrast, for $y > 90$ mm, these over-intensities are not observed anymore. These over-intensities are known to be representative of OH super-equilibrium concentrations in the vicinity of the flame front (Yamamoto et al., 2009). A criterion is implemented to divide this interface into two zones: the flame front (visible in Fig. 4) and another downstream segmentation line probably depicting an interface between fresh and burnt gases (Zentgraf et al., 2021). The flame front in Fig. 4a is colored by the flame curvature, κ_c , determined with the curvilinear coordinates (z, y) of the flame

front as (Poinsot et al., 2011; Hsu et al., 2021)

$$\kappa_c = \nabla \cdot \mathbf{n} = \frac{\dot{z}\dot{y} - \ddot{z}\dot{y}}{(\dot{z}^2 + \dot{y}^2)^{1.5}}, \quad (2)$$

where \vec{n} is the unit vector normal to the flame front and points towards fresh gases and $(\dot{\cdot})$ indicates the derivative, estimated with a Savitzky-Golay local polynomial fit Hsu et al. (2021). κ_c indicates to which extent the flame is curved, the sign convention being in accordance with the increase of the flame stretch (κ_c is negative when the flame front is concave towards fresh gases (Poinsot et al., 2011; Law, 2006)). When $M = 0.5$ (Fig. 4a), the cooling air film only marginally influences the flame dynamics, which presents two typical features. When the flame front is close to the wall, κ_c is always positive, with the presence of large-scale bulbs. In the other hand, highly curved finger-like structures are observed far away from the wall with negative curvatures. These two features have already been reported in the literature and are typical from classical side-wall quenching with V-shaped flames (Zentgraf et al., 2021; Kheirkhah & Gülder, 2013). The flame front in Fig. 4b is colored by the flame strain rate, κ_s , defined as

$$\kappa_s = \nabla_t \cdot \mathbf{u} = (1 - n_z^2) \frac{\partial u_z}{\partial z} + (1 - n_y^2) \frac{\partial u_y}{\partial y} - n_z n_y \left(\frac{\partial u_z}{\partial y} + \frac{\partial u_y}{\partial z} \right), \quad (3)$$

where u_y and u_z are the flow velocity components extracted from PIV data along the flame front, and \mathbf{n} is the unit vector normal to the flame front. κ_s gives another indication of how the flow heterogeneity stretches the flame front. When κ_s is negative, the flow contracts the flame front, and reduces its area. Evolution of κ_s for $M = 3$ (Fig. 4b) depicts a more corrugated flame front above the lip ($y > 60$ mm) with high values of positive and negative κ_c , highlighting the presence of a shear layer between the cooling air film and the mainstream flow. Because the flame front interacts with this shear layer with its own dynamics, it experiences either an expansion or a contraction.

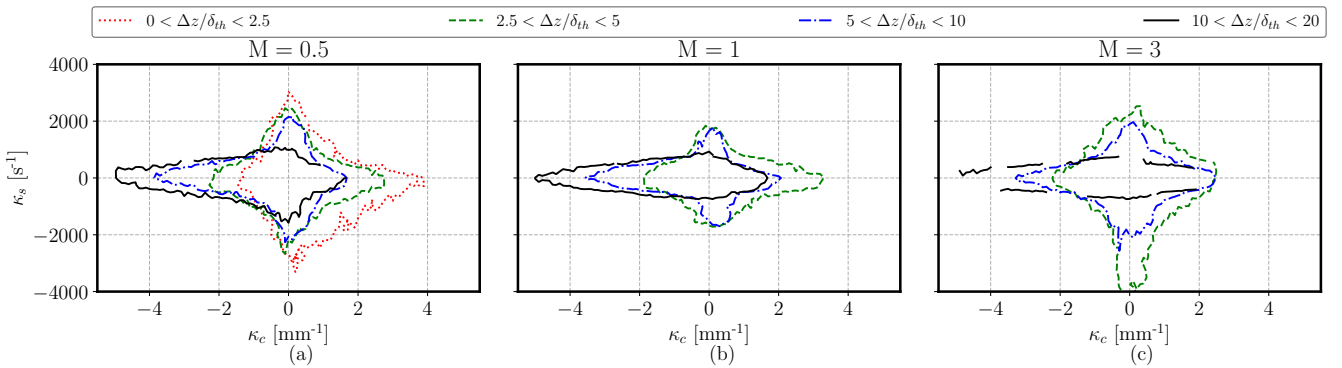


Figure 5. Joint PDFs (contour at 5×10^{-7}) between the flame strain rate, κ_s (Eq. 3), and the flame curvature, κ_c (Eq. 2), conditioned by four bins of the normalized flame-to-wall distance, $\Delta z / \delta_{th}$, for (a) $M = 0.5$, (b) $M = 1$ and (c) $M = 3$.

In order to spatially correlate the effect of curvature, κ_c and flow strain, κ_s , Fig. 5 shows the joint PDFs between κ_s and κ_c , that are sorted according to the normalized flame-to-wall distance Δ / δ_{th} (δ_{th} is the thermal flame thickness (Mazellier et al., 2010)). Overall, the cross shape along the main directions of these PDFs highlights the fact that the flame is wrinkled either by curvature or flow

strain. When $M = 0.5$, the PDFs feature an evolution with regards to the location to the wall (Fig. 4(a)). For $z/\delta_{th} < 2.5$, the flame is mostly curved with positive values, being in agreement with the bulbs observed in Fig. 4a. When the flame is away from the wall, the effects of κ_c and κ_s are balanced and when $z/\delta_{th} > 5$, the flame is more and more negatively curved while κ_s is negligible. The presence of finger-like structures occurs far away from the wall and are visible in the PDFs while flow strain generated by the cooling air film is not preponderant in these regions. The κ_c - κ_s correlation for $M = 3$ highlights an important negative flame strain in the $2.5 < \Delta z/\delta_{th} < 10$ region. The detailed analysis of κ_s shows the predominance of the $\partial u_y/\partial z$ shear term. Since the FF still exists up to $y = 90$ mm (flame brush in Fig. 2c), it seems that the FF is located in the outer region of the shear layer, dominated by compressive strain rates, and where fresh unburnt gases can feed the FF without significant dilution that could lower the local equivalence ratio.

In order to investigate how the developing shear layer influences the flame front reactivity via a combination of heat losses and wall-bounded turbulence, the flame dilatation, \mathcal{D} , is a valuable scalar that informs on the level of heat generation through the front, being estimated solely with the velocity fields as

$$\mathcal{D} = \nabla \cdot \mathbf{u} = \frac{\partial u_z}{\partial z} + \frac{\partial u_y}{\partial y}. \quad (4)$$

\mathcal{D} is positive when combustion takes place and tends to zero at the wall (Zhao et al., 2018). Being unable to probe the thermochemical state of the gas phase, the estimation of \mathcal{D} is possible only with the reactive PIV data.

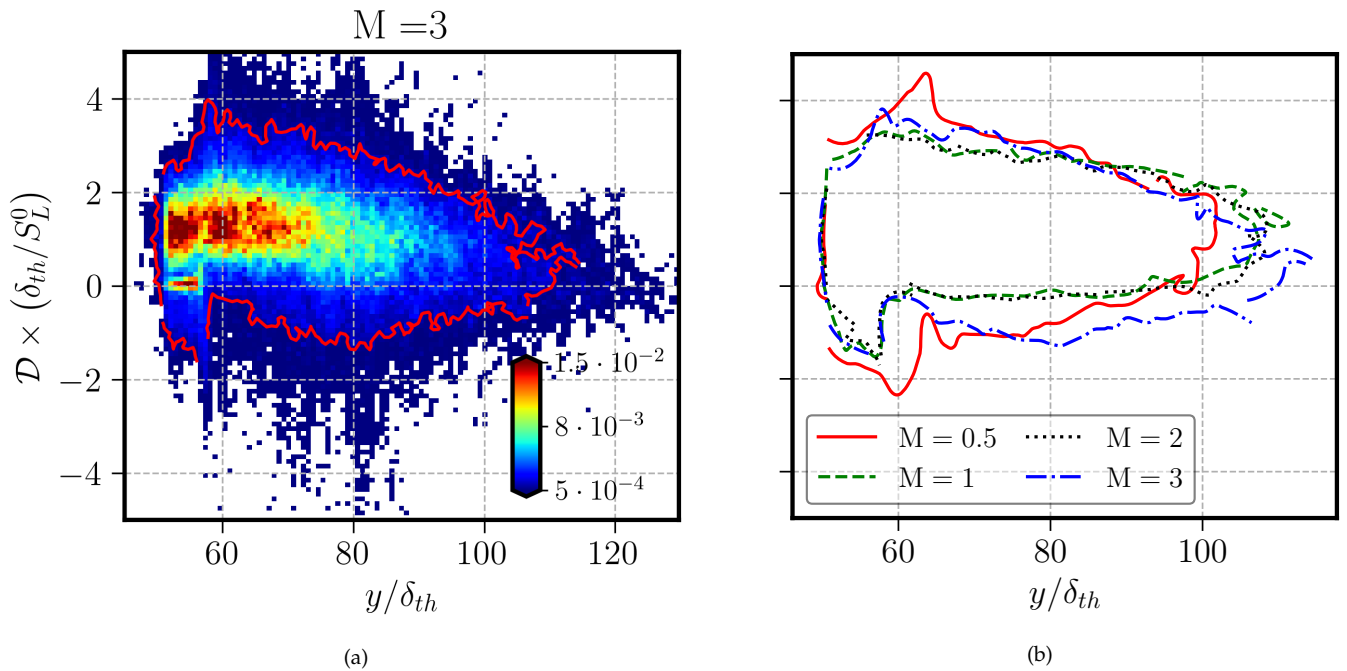


Figure 6. Joint PDFs (blue-to-red color scale and red contour at 1×10^{-3}) between the normalized flame dilatation, \mathcal{D} (Eq. 4), and the normalized streamwise direction, y/δ_{th} . (a) PDF for $M = 3$. (b) Iso-probability contours for different

Figure 6 shows the joint PDFs between \mathcal{D} and the normalized streamwise distance, y/δ_{th} . \mathcal{D} presents a small area of null values nearby the lip for $M = 0.5$ and $M = 1$ (Figs 6b). Indeed, the weak cooling air momentum seems to quench the FF in a reduced region before the heat generation overtakes. Further downstream, \mathcal{D} is constantly positive. The trend for $M = 3$ (Fig. 6a) is slightly differing since \mathcal{D} drops to zero for $y/\delta_{th} > 75$. This trend is corroborated with the above-mentioned analysis, originating from the combined effects of flame strain, heat losses, and mixing, that could affect the inner flame structure (Poinsot et al., 2011; Law, 2006).

4. Conclusions

The interaction between a V-shaped lean turbulent premixed methane-air flame and a parietal cooling air film is experimentally studied for various blowing ratios (M). Simultaneous OH-PLIF, reactive PIV and surface PT are applied to obtain correlations between the flame structure, the aerodynamics and the wall temperature. The increase of the cooling air film momentum shifts the flame brush away from the wall, but also enable a better control of the wall thermal stress and the flame wrinkling. Specifically, when $M < 1$, the air film has a limited influence on the flame dynamics so that a common flame-wall interaction process is retrieved. The important heat losses induces great variations of the wall temperature and also affect the adiabatic feature of flames. Conversely, When $M > 1$, the air film sustains along the wall and the flame is located in the outer region of the developing shear layer, being influenced by compressive strain rates and heat losses to the air film. 3D effects and mixing will be carefully addressed in the near future.

Acknowledgements

Financial support was provided by the project WALL-EE of the French National Research Agency (ANR), grant no. ANR-19-CE05-0007.

References

- Ahmed, S., Ramakrishnan, K. R., & Ekkad, S. V. (2021). Overall cooling effectiveness of effusion cooled can combustor liner under reacting and non-reacting conditions. *J. Therm. Sci. Eng. Appl.*, *14*(2), 021009.
- Aldén, M., Omrane, A., Richter, M., & Särner, G. (2011). Thermographic phosphors for thermometry: A survey of combustion applications. *Progress in Energy and Combustion Science*, *37*(4), 422–461.
- Alshaalan, T., & Rutland, C. J. (2002). Wall heat flux in turbulent premixed reacting flow. *Combust. Sci. Technol.*, *174*(1), 135–165.

- Behrendt, T., Lengyel, T., Hassa, C., & Gerendàs, . M. (2008, 06). Characterization of advanced combustor cooling concepts under realistic operating conditions. In *Turbo expo: Power for land, sea, and air* (Vols. Volume 4: Heat Transfer, Parts A and B, pp. 1801–1814).
- Bogard, D. G., & Thole, K. A. (2006). Gas turbine film cooling. *Journal of Propulsion and Power*, 22(2), 249–270.
- Bruneaux, G., Poinot, K. A. T., & Ferziger, J. H. (1996). Flame-wall interaction simulation in a turbulent channel flow. *Combust. Flame*, 107(1-2), 27–44.
- Dreizler, A., & Böhm, B. (2015). Advanced laser diagnostics for an improved understanding of premixed flame-wall interactions. *Proceedings of the Combustion Institute*, 35(1), 37–64.
- Feist, J. P., Heyes, A. L., & Seefelt, S. (2003). Thermographic phosphor thermometry for film cooling studies in gas turbine combustors. *Proceedings of the Institution of Mechanical Engineers, Part A: Journal of Power and Energy*, 217(2), 193–200.
- Fischer, L., Breda, P., Dalshad, R., & Pfitzner, M. (2021). Numerical characterization of a novel test bench featuring secondary reactions of methane. *Aerosp. Sci. Technol.*, 107203.
- Foucher, F., Burnel, S., Mounaïm-Rousselle, C., Boukhalfa, M., Renou, B., & Trinite, M. (2003). Flame wall interaction: effect of stretch. *Exp. Therm. Fluid Sci.*, 27(4), 431–437.
- Ganter, S., Heinrich, A., Meier, T., Kuenne, G., Jainski, C., Reißmann, M. C., ... Janicka, J. (2017). Numerical analysis of laminar methane–air side-wall-quenching. *Combust. Flame*, 186, 299–310.
- Goodwin, D. G., Speth, R. L., Moffat, H. K., & Weber, B. W. (2021). *Cantera: An object-oriented software toolkit for chemical kinetics, thermodynamics, and transport processes*. <https://www.cantera.org>. (Version 2.5.1)
- Greifenstein, M., & Dreizler, A. (2021). Investigation of mixing processes of effusion cooling air and main flow in a single sector model gas turbine combustor at elevated pressure. *International Journal of Heat and Fluid Flow*, 88, 108768.
- Greifenstein, M., Hermann, J., Boehm, B., & Dreizler, A. (2019). Flame–cooling air interaction in an effusion-cooled model gas turbine combustor at elevated pressure. *Experiments in Fluids*, 60(1), 10.
- Gruber, A., Sankaran, R., & E. R. Hawkes, J. H. C. (2010). Turbulent flame–wall interaction: a direct numerical simulation study. *J. Fluid Mech.*, 658, 5–32.
- Gustafsson, K. M. B., & Johansson, T. G. (2001, 01). An Experimental Study of Surface Temperature Distribution on Effusion-Cooled Plates . *Journal of Engineering for Gas Turbines and Power*, 123(2), 308–316.

- Hermann, J., Greifenstein, M., Boehm, B., & Dreizler, A. (2019). Experimental investigation of global combustion characteristics in an effusion cooled single sector model gas turbine combustor. *Flow, Turbulence and Combustion*, 102(4), 1025–1052.
- Hsu, P. S., Jiang, N., Lauriola, D., Grib, S. W., Schumaker, S. A., Caswell, A. W., & Roy, S. (2021, May). 10 khz 2d thermometry in turbulent reacting flows using two-color oh planar laser-induced fluorescence. *Appl. Opt.*, 60(15), C1–C7.
- Jainski, C., Reißmann, M., Böhm, B., Janicka, J., & Dreizler, A. (2017). Sidewall quenching of atmospheric laminar premixed flames studied by laser-based diagnostics. *Combust. Flame*, 183, 271–282.
- Kheirkhah, S., & Gülder, Ö. L. (2013). Turbulent premixed combustion in v-shaped flames: Characteristics of flame front. *Phys. Fluids*, 25(5), 055107.
- Kumar, K. R. Y., Qayoum, A., Saleem, S., & Qayoum, F. (2020, apr). Effusion cooling in gas turbine combustion chambers - a comprehensive review. *IOP Conference Series: Materials Science and Engineering*, 804(1), 012003.
- Lange, L., Heinze, J., Schroll, M., Willert, C., & Behrendt, T. (2012). Combination of planar laser optical measurement techniques for the investigation of pre-mixed lean combustion, 16th int. In *Symposium on applications of laser techniques to fluid mechanics, lisbon, portugal*.
- Law, C. K. (2006). *Combustion physics*. Cambridge University Press.
- Lefebvre, A. H., & Ballal, D. R. (2010). *Gas turbine combustion: alternative fuels and emissions*. CRC press.
- Mann, M., Jainski, C., Euler, M., Böhm, B., & Dreizler, A. (2014). Transient flame–wall interactions: Experimental analysis using spectroscopic temperature and co concentration measurements. *Combust. Flame*, 161(9), 2371–2386.
- Mazellier, N., Danaila, L., & Renou, B. (2010). Multi-scale energy injection: a new tool to generate intense homogeneous and isotropic turbulence for premixed combustion. *Journal of Turbulence*, 11, N43.
- Mendez, S., & Nicoud, F. (2008). Large-eddy simulation of a bi-periodic turbulent flow with effusion. *Journal of Fluid Mechanics*, 598, 27–65.
- Palulli, R., Brouzet, D., Talei, M., & Gordon, R. (2021). A comparative study of flame-wall interaction and flame-cooling air interaction. *Int. J. Heat Fluid Flow*, 92, 108888.
- Palulli, R., Talei, M., & Gordon, R. L. (2021). Analysis of near-wall CO due to unsteady flame–cooling air interaction. *Flow Turb. Combust.*, 107, 343–365.

- Picchi, A., Andreini, A., Becchi, R., & Facchini, B. (2020, 09). *A New Test Facility for Investigating Thermal Behaviour of Effusion Cooling Test Plates for RQL Combustors* (Vol. Volume 7A: Heat Transfer). (V07AT11A013)
- Poinsot, T., Garcia, M., Senoner, J. M., Gicquel, L., & Vermorel, O. (2011). Numerical and physical instabilities in massively parallel les of reacting flows. *Journal of Scientific Computing*, 49, 78–93.
- Rivera, J. E., Gordon, R. L., Brouzet, D., & Talei, M. (2019). Exhaust CO emissions of a laminar premixed propane–air flame interacting with cold gas jets. *Combust. Flame*, 210, 374–388.
- Sivasegaram, S., & Whitelaw, J. H. (1969). Film cooling slots: The importance of lip thickness and injection angle. *Journal of Mechanical Engineering Science*, 11(1), 22-27.
- Sotton, J., Boust, B., Labuda, S. A., & Bellenoue, M. (2005). Head-on quenching of transient laminar flame: Heat flux and quenching distance measurements. *Combustion Science and Technology*, 177(7), 1305–1322.
- Yamamoto, K., Ozeki, M., Hayashi, N., & Yamashita, H. (2009). Burning velocity and oh concentration in premixed combustion. *Proc. Combust. Inst.*, 32(1), 1227–1235.
- Zentgraf, F., Johe, P., Cutler, A. D., Barlow, R. S., Böhm, B., & Dreizler, A. (2021). Classification of flame prehistory and quenching topology in a side-wall quenching burner at low-intensity turbulence by correlating transport effects with co₂, co and temperature. *Combustion and Flame*, 111681.
- Zhao, P., Wang, L., & Chakraborty, N. (2018). Analysis of the flame–wall interaction in premixed turbulent combustion. *Journal of Fluid Mechanics*, 848, 193–218.